

Observations and Simulations of Relativistic Jets

José-Luis Gómez

Instituto de Astrofísica de Andalucía (CSIC), Apartado 3004, Granada 18008, Spain

Abstract. The recent improvement in VLBI arrays is providing information of the emission and magnetic field structure of relativistic jets, both extragalactic and galactic (microquasars), with unprecedented spatial and temporal resolution. These observations are revealing the importance of the hydrodynamical processes that govern the jet evolution, which can be studied by the recently developed time-dependent relativistic hydrodynamical models. Computation of the non-thermal emission from these hydrodynamical models, and its comparison with actual sources, is proving as one of the most powerful tools in the understanding of the physical processes taking place in these jets. This paper reviews some of the recent observational results, as well as the numerical models used to interpret them.

1 Introduction

Since the classical works of [11] and [13], our knowledge of the jet physics in AGNs and microquasars have improved significantly by analytical and numerical models. The analytical efforts provided the basic frame work to understand the non-thermal synchrotron and inverse Compton emission of inhomogeneous jets ([93], [85]); spectral evolution of shock waves, associated with the superluminal components ([12], [94], [63]); and polarization (e.g., [20]). The implementation of these analytical results into numerical models have allowed testing of the basic jet model hypotheses, as well as a more detailed comparison with the observations ([70], [64], [65], [43], [44], [45]). However, these early numerical models are limited by the lack of a detailed non-linear model to study the relativistic jet dynamics, being forced to adopt simplified stationary relativistic hydrodynamical models.

On the other hand, Newtonian hydrodynamical numerical models have been used to obtain a more detailed study of the jet dynamics, and its influence in the jet observational properties. These models explored with great success the morphology, dynamics and stability of jets (see e.g. reviews [109], [27]), mainly aimed to study the large scale jet structure. However, these models cannot account for the relativistic effects that are of special importance in the overall emission of jets in AGNs and microquasars.

First studies of relativistic (magneto)hydrodynamical jets were obtained for stationary flows ([136], [24], [17]). A significant step forward in the field of numerical simulations came with the development of modern high-resolution techniques in numerical hydrodynamics, making feasible the computation of time-dependent simulations of relativistic jets ([127], [99], [100], [102], [25], [83], and reviews [101], [103], [104], [7]). These models are capable, for the first time, to

study the jet dynamics with unprecedented detail, and under very similar conditions as it is thought are taking place in real sources (strong shocks, relativistic internal energies and bulk flow velocities, etc.). Some of the latest simulations have started to explore three dimensional relativistic jets ([4], [5], [6], [59]), magnetized relativistic jets ([84]), as well as jet formation and collimation making use of the first general relativity magnetohydrodynamical codes ([79], [80], [81], [105], [106]).

However, The emission structure that we observe in our VLBI images is not just a direct mapping of the jet hydrodynamical variables (pressure, density, velocity). The final radiation reaching our detectors is greatly determined by other several processes, like Faraday rotation, opacity, particle acceleration, radiative losses, and, most importantly, by relativistic effects such as light aberration and light travel time delays. For relativistic speeds (and small viewing angles) time delays can be of such importance as to render the emission images with no apparent relationship to the hydrodynamical jet structure. Therefore, the state of the art in the simulation of relativistic jets involves the computation of the emission, taking into account the appropriate relativistic and transfer of radiation processes, from the relativistic time-dependent hydrodynamical results ([46], [47], [48], [49], [66], [82], [107], [83], [5], [6], [71], [1], and review [57]). Comparison of these simulations with actual observations should provide a better understanding of the relativistic jets in AGNs and microquasars.

2 Relativistic HD and Emission models

Most of the energy transported in relativistic jets is assumed to be carried out by a population of thermal electrons. This population determines the hydrodynamical evolution of the jet, and can be simulated by the relativistic HD codes. However, the non-thermal emission observed from these jets is originated by a second population of high energy, non-thermal particles. Detection of circular polarization in the jet of 3C 279 ([133]), as well as in 3C 84, PKS 0528+134, and 3C 273 ([60]), suggests that this non-thermal population is mainly composed by pairs electron–positron. It is still unclear how this non-thermal population is originated ([96]), perhaps by pair cascades ([91], [14]), neutron decay ([26], [42]), or by acceleration of the thermal electrons at a strong recollimation shock presumably associated with the VLBI core ([22], [98], [89], [90]). This population of non-thermal electrons is subsequently re-accelerated at shocks along the jet ([77], [38], [78], [39]), and incremented with contributions from thermal electrons accelerated at the same shocks.

In order to compute the expected emission from the hydrodynamical models is necessary to establish a relationship between the thermal and non-thermal jet populations. A common assumption considers that the particle and energy density of the non-thermal electrons is a constant fraction of the thermal electrons ([113], [135], [46], [49], [6], [107], [83]). The population of non-thermal electrons is assumed to share the same dynamics as the thermal population, which can therefore be computed using the hydrodynamical simulations. Any exchange be-

tween internal and kinetic energy along the jet will maintain the proportionality between thermal and non-thermal populations. Only non-adiabatic processes, such as gains by particle acceleration in shocks or losses by radiation can modify this proportionality.

Radiative losses at radio wavelengths are expected to be small, except at strong shocks, such as the terminal hot spots and jet cocoon. It is therefore expected that computation of parsec scale radio emission will not be severely influenced by changes in the non-thermal population produced by radiative losses or particle accelerations. At higher energies (i.e., optical) and at sites of strong shocks it is possible to trace the electron non-thermal population gains and losses of energy by computing the electron energy transport during the jet evolution. This has been recently considered for non-relativistic magnetohydrodynamic simulations ([71]), allowing the exploration of the effects induced in the emission by synchrotron aging and electron energy gains at strong shocks.

To compute the synchrotron emission is necessary to distribute the internal energy calculated from the hydrodynamic codes among the relativistic non-thermal electrons. This is done by assuming a power law energy distribution in the form $N(E)dE = N_o E^{-\gamma} dE$, with $E_{min} \leq E \leq E_{max}$, and spectral index γ . Neglecting radiative energy losses and particle accelerations, the ratio C_E between the maximum and minimum energy remains constant through the computational domain and can be considered a free parameter of the model. The power law is then fully determined by the equation ([46])

$$N_o = \left[\frac{U(\gamma - 2)}{1 - C_E^{2-\gamma}} \right]^{\gamma-1} \left[\frac{1 - C_E^{1-\gamma}}{N(\gamma - 1)} \right]^{\gamma-2} \quad (1)$$

and

$$E_{min} = \frac{U \gamma - 2}{N \gamma - 1} \frac{1 - C_E^{1-\gamma}}{1 - C_E^{2-\gamma}} \quad (2)$$

where U and N represent the electron energy density and number density, respectively, as calculated by the hydrodynamical codes.

It is still largely unknown what may be the role played by the magnetic field in the jet dynamics of AGNs and microquasars. There are some evidence pointing towards a small contribution of the magnetic field in the dynamics ([67]), although only future observations and magnetohydrodynamical simulations ([24], [128], [84], [80]) could answer this question. So far, and mainly due to the fact that the emission computations have been performed for purely hydrodynamical models, the magnetic field has been assumed to be dynamical negligible, with a magnetic energy density proportional to the particle energy density ([135]), leading to a field with magnitude proportional to \sqrt{U} . Once the magnetic field is considered dynamically negligible, ad-hoc magnetic field structures can be considered. To account for the small degree of linear polarization observed in many sources, the magnetic field is commonly considered to be predominantly turbulent.

2.1 Synchrotron Radiation Transfer

The transfer of synchrotron radiation have been considered in detail previously under different astrophysical scenarios, see e.g., [111], [68], [69], [64]. Its implementation for computing the polarized emission from the hydrodynamical models can be summarized as follows ([43], [44], [45], [46]).

To obtain the emission and absorption coefficients for the transfer of polarized synchrotron radiation let consider the direction of the component of the magnetic field in the plane of the sky at a given computational cell be specified as direction 2, and let the axis 1, 2, and the direction toward the observer be directions which form a right-handed orthogonal system in that order. In this system, the emission and absorption coefficients, respectively, are then computed *in the fluid frame* using (see e.g., [111])

$$\varepsilon_{\nu}^{(i)} = \frac{\sqrt{3}}{16\pi} \frac{e^3}{mc^2} C_1^{(\gamma-1)/2} N_o (B \sin \vartheta)^{(\gamma+1)/2} \nu^{(1-\gamma)/2} \int_{x_{min}}^{x_{max}} x^{(\gamma-3)/2} [F(x) \pm G(x)] dx \quad (3)$$

$$\kappa_{\nu}^{(i)} = \frac{\sqrt{3}e^3}{16\pi m} (\gamma + 2) C_1^{\gamma/2} N_o (B \sin \vartheta)^{(\gamma+2)/2} \nu^{-(\gamma+4)/2} \int_{x_{min}}^{x_{max}} x^{(\gamma-2)/2} [F(x) \pm G(x)] dx \quad (4)$$

where the plus sign is to be taken for $i=1$, and the minus sign is valid for $i=2$; ϑ is the angle between the magnetic field and the line of sight; and

$$C_1 = \frac{3e}{4\pi m^3 c^5}$$

$$x = \frac{\nu}{C_1 B \sin \vartheta E^2}$$

$$F(x) = x \int_x^{\infty} K_{5/3}(z) dz$$

$$G(x) = x K_{2/3}(x)$$

where $K_{5/3}$ and $K_{2/3}$ are the corresponding Bessel functions.

If the distribution of the magnetic field within the source is not uniform in orientation the (1, 2) system will differ from cell to cell, thus it is more convenient to formulate the transfer equations in a system (a, b) , which is fixed in orientation with respect to the observer. The relative orientation of the axis 2 with respect to the axis a , which defines the angle χ_B , will change from cell to cell as the magnetic field does.

The radiation field is characterized by the four Stokes parameters I , Q , U , and V , or equivalently by $I^{(a)}$, $I^{(b)}$, U , and V , where $I = I^{(a)} + I^{(b)}$ and $Q =$

$I^{(a)} - I^{(b)}$. Provided jets in blazars exhibit very low circular polarization we can assume $V = 0$. I is the total intensity, and Q and U determine the degree of polarization

$$\Pi = (Q^2 + U^2)^{1/2}$$

and the polarization position angle

$$\chi = \frac{1}{2} \arctan\left(\frac{U}{Q}\right).$$

The change of the parameters $I^{(a)}$, $I^{(b)}$ and U characterizing the radiation passing through a volume element of length ds can be obtained by solving the transfer equations in the $(1, 2)$ system and transforming to the (a, b) system, given by

$$\begin{aligned} \frac{dI^{(a)}}{ds} = I^{(a)} & \left[-\kappa_\nu^{(1)} \sin^4 \chi_B - \kappa_\nu^{(2)} \cos^4 \chi_B - \frac{1}{2} \kappa_\nu \sin^2 2\chi_B \right] \\ & + U \left[\frac{1}{4} (\kappa_\nu^{(1)} - \kappa_\nu^{(2)}) \sin 2\chi_B + d\chi_F/ds \right] \\ & + \varepsilon_\nu^{(1)} \sin^2 \chi_B + \varepsilon_\nu^{(2)} \cos^2 \chi_B \end{aligned} \quad (5)$$

$$\begin{aligned} \frac{dI^{(b)}}{ds} = I^{(b)} & \left[-\kappa_\nu^{(1)} \cos^4 \chi_B - \kappa_\nu^{(2)} \sin^4 \chi_B - \frac{1}{2} \kappa_\nu \sin^2 2\chi_B \right] \\ & + U \left[\frac{1}{4} (\kappa_\nu^{(1)} - \kappa_\nu^{(2)}) \sin 2\chi_B - d\chi_F/ds \right] \\ & + \varepsilon_\nu^{(1)} \cos^2 \chi_B + \varepsilon_\nu^{(2)} \sin^2 \chi_B \end{aligned} \quad (6)$$

$$\begin{aligned} \frac{dU}{ds} = I^{(a)} & \left[\frac{1}{2} (\kappa_\nu^{(1)} - \kappa_\nu^{(2)}) \sin 2\chi_B - 2 d\chi_F/ds \right] \\ & + I^{(b)} \left[\frac{1}{2} (\kappa_\nu^{(1)} - \kappa_\nu^{(2)}) \sin 2\chi_B + 2 d\chi_F/ds \right] \\ & - \kappa_\nu U - (\varepsilon_\nu^{(1)} - \varepsilon_\nu^{(2)}) \sin 2\chi_B \end{aligned} \quad (7)$$

with the average $\kappa_\nu = (\kappa_\nu^{(1)} + \kappa_\nu^{(2)})/2$. The derivative $d\chi_F/ds$ represents the change of the plane of polarization per unit distance ds due to Faraday rotation.

A simpler formulation for the transfer of synchrotron radiation can be obtained when neglecting the different polarizations ([107]). For the total intensity, the emission and absorption coefficients can be computed using, respectively

$$\varepsilon_\nu \propto p^{(\alpha+3)/2} \nu^{-\alpha} \quad (8)$$

$$\kappa_\nu \propto p^{(2\alpha+7)/2} \nu^{(\alpha+5/2)} \quad (9)$$

being p the thermal pressure and α the spectral index. The total intensity can then be integrated using ([19])

$$I = I_0 e^{-\tau_\nu} + \frac{\varepsilon_\nu}{\kappa_\nu} (1 - e^{-\tau_\nu}) \quad (10)$$

where τ_ν is the optical depth.

Further simplifications can be considered by ignoring opacity effects, in which case an estimation of the total intensity emission can be obtained just by adding the emission coefficient (Eq. 8) along the different cells in the line of sight ([83]).

2.2 Relativistic Effects

The presence of emitting gas at velocities close to that of the speed of light enhance the importance of the relativistic effects in the final emission structure of the simulated maps. The emission and absorption coefficients to be used in Eqs. (5-7) are those transformed into the observer's frame using the standard Lorentz transformations

$$\varepsilon_{\nu^{ob}}^{ob} = \delta^2 \varepsilon_\nu \quad (11)$$

$$\kappa_{\nu^{ob}}^{ob} = \delta^{-1} \kappa_\nu \quad (12)$$

where $\delta = \Gamma^{-1}(1 - \beta \cos \theta)^{-1} = \nu^{ob}/\nu$ is the Doppler factor; θ the viewing angle; β the flow velocity in units of the speed of light; and Γ the flow bulk Lorentz factor. Note that light aberration (see e.g., [116]) changes the orientation of the line of sight as seen in the fluid's frame, and therefore the relative orientation of the magnetic field and line of sight as seen in the fluid frame, ϑ . The emission and absorption coefficients are a function of $\sin \vartheta$ (Eqs. 3 and 4), and therefore light aberration can significantly affects the synchrotron total and polarized emission as a function of the flow velocity or viewing angle (see section 5.2).

Besides light aberration, time delays is the most important effect determining the final emission structure (no superluminal motions can be obtained from these simulations without considering the time delays between different jet regions). Provided the hydrodynamical variables are cell and time dependent, to account for delays within the jet is necessary to compute the emission and absorption coefficients at a retarded time, given by

$$\tau = t - \frac{\vec{x} \cdot \vec{l}}{c} \quad (13)$$

where \vec{x} is the position vector of the cell, \vec{l} denotes the line of sight unity vector, and c is the speed of light.

We can investigate the observational consequences of light travel delays by considering the effects produced in the emission of shocked jet material ([95], [45]). Because of the time delays between the far and near sides of a shock front, it appears rotated in the observed frame by an angle $\arccos \beta$. Depending on the pattern velocity of the shock front and viewing angle, time delays have a tendency

towards aligning the shock front with the visual. This may have relevant effects in the emission time variability of material being heated by a shock by producing a “phasing” effect of the emission as measured by the observed, thus allowing for very rapid variability ([117]).

Light travel delays between the forward and reverse shocks produce a lengthening of the shocked material region in the observers frame by a factor $\sin\theta/(1 - \beta \cos\theta)$ ([45], [41]). Therefore, it is possible to obtain estimations of the shocked material size in the source frame from the measured sizes, velocities, and viewing angles of superluminal components. High resolution VLBI observations ([72], [50], [52], [89], [56], [37]) reveal components sizes in some cases of the order of the jet width. If we assume commonly estimated values of $\Gamma \sim 10$ and $\theta = 10^\circ$, this implies that the emitting material associated with the superluminal component must be $\sim 1/9$ smaller than the jet width. Thus, either shocks are very thin in the source frame, or radiative losses limit the emitting region in shocks to a thin layer ([97]). It is also possible that, instead, multiple superluminal components may be associated with a single moving shock (see section 3.1).

3 Hydrodynamical Models of Superluminal Sources

Shock-in-jet models ([12], [94], [63]) have been proven to provide a general explanation for the emission variability observed in components of relativistic jets. Numerical relativistic HD and emission simulations provide a new powerful tool to improve upon these previous analytical models. With these new numerical techniques it is now possible to study with great detail the generation, structure, and evolution of strong shocks, and analyze its importance in the overall dynamical evolution and emission of jets through comparison with recent high resolution VLBI observations.

3.1 Relativist Shocks

Superluminal components as associated with moving shock waves have been studied by relativistic hydrodynamical and emission models ([49], [83], [107]). In these models, moving shocks are induced by the introduction of perturbations in steady relativistic jets, studying the subsequent jet evolution.

In [49] the fluid jet dynamics are computed using a relativistic, axially-symmetric jet model obtained by means of a high-resolution shock capturing scheme ([100], [102]) to solve the equations of relativistic hydrodynamics in cylindrical coordinates. The jet material is represented by an ideal gas of adiabatic exponent $4/3$ and the quiescent state corresponds to a diffuse ($\rho_b/\rho_a = 10^{-3}$), relativistic ($\Gamma_b = 4$), overpressured ($p_b = 3p_a/2$), cylindrical beam with (local) Mach number $M_b = 1.69$ (subscripts a and b refer, respectively, to atmosphere and beam). The jet propagates through a pressure-decreasing atmosphere which allows the jet to expand radially. The initial pressure mismatch in the model causes recollimation shocks and expansions in the jet flow ([46]). The formation and evolution of shock waves is studied by introducing a square-wave increase

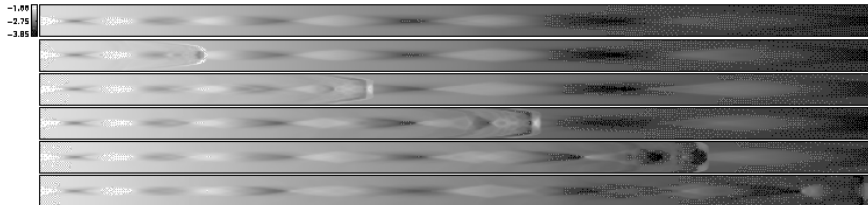


Fig. 1. Pressure distribution at six epochs (0 to $200 R_b/c$ in steps of 40) after the introduction of a square-wave perturbation to the flow Lorentz factor for the jet model discussed in the text. The simulation has been performed over a grid of 1600×80 cells, with a spatial resolution of 8 cells/ R_b in both radial and axial directions. Reprinted from [49].

of the beam flow velocity from the quiescent value $\Gamma_b = 4$, to $\Gamma_p = 10$ during a short period of time $\tau_p = 0.75 R_b/c$. Because of the faster flow velocity in the perturbation, the fluid in front piles up, creating a shocked state, which is trailed by a rarefaction.

The resulting dynamical evolution of the perturbation along the jet is shown in Fig. 1, which contains a set of panels showing the pressure distribution at different epochs. The first panel corresponds to the quiescent jet. Both the shocked and rarefied regions in the perturbation are clearly seen. When the perturbation passes through a standing shock, the latter is “dragged” downstream for some distance before returning to its initial position as the steady jet becomes reestablished.

Figure 2 shows the total intensity maps corresponding to the stationary model (top panels), and four epochs in the evolution of the disturbance along the jet. Left and right image sequences of Fig. 2 represent the same data, but with different components identification. By looking at the unconvolved stationary total intensity image we observe a regular pattern of knots of high emission, associated with the increased specific internal energy and rest-mass density of internal oblique shocks produced by the initial overpressure in this model. VLBI cores can be interpreted as a first strong recollimation shock in the steady jet ([22], [98], [46], [89]). The regular pattern of knots should remain constant in flux and position as long as the jet inlet hydrodynamical variables remain unchanged. Therefore, these components resulting from the recollimation shocks may represent an alternative explanation for the stationary jet components commonly observed in many sources ([86], [134], [72], [53], [55]) as opposed to jet bendings ([2], [51]).

The time evolution of the convolved maps in Fig. 2 shows the usual core-jet VLBI structure of a blazar, with a single well-defined traveling component associated with the moving shock. The unconvolved maps show a much more complex jet structure. Due to time delays, the shocked region appears as a very extended region of higher emission (see section 2.2), which is moving and interacting with the quiescent jet. A tentative identification of components through

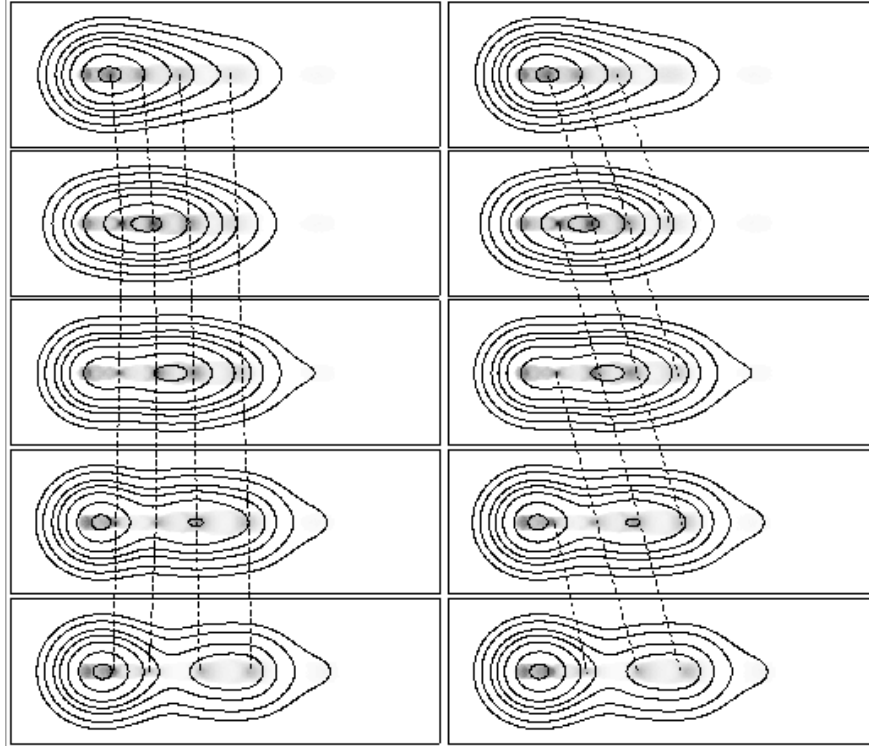


Fig. 2. Simulated total intensity maps of the hydrodynamical model presented in Fig. 1 at five different epochs. Both, left and right image sequences, represent the same data but with different components identification (see text). Grey scale (normalized to the maximum of all five epochs) shows the emission maps with the full resolution provided by the simulations. Contours show the same images once convolved with a Gaussian beam to resemble actual VLBI observations. Top panels show the stationary model. Maps are obtained for an optically thin observing frequency, and a viewing angle of 10° . Reprinted from [49].

epochs is shown in the right sequence of images of Fig. 2, where components are connected by dashed lines. Without further information from the simulations, this would seem the most plausible identification of components, since it would conclude the existence of multiple superluminal components with similar apparent motions to that of the main single superluminal component obtained by analyzing the lower resolution images, that is, the convolved maps. However, this identification of components is completely wrong. When analyzing the simulations through intermediate epochs to those shown in Fig. 2 we obtain the correct identification of components, marked on the left sequence of images of Fig. 2. This shows the importance of a well time sampled monitoring when studying and identifying superluminal components through epochs. It puts in evidence how easily a wrong identification of components may result from a sparse time

monitoring. Most of the information obtained from analyzing VLBI images is deduced from the measured apparent motions, which, as shown here, may easily be completely wrong, and so the obtained conclusions.

By analyzing the structural changes in the correctly identified images of Fig. 2 we observe that the interaction of the moving shock with the underlying jet produces a temporary “dragging” of the previously stationary features, accompanied by an increase in their fluxes. Components later on come to a stop, followed by upstream motions of the inner components. This upstream motion does not represent actual upstream movement of the jet fluid, but a re-positioning of the recollimation shock closer to the jet inlet.

As the images of Fig. 2 show, detection of this predicted dragging and upstream motion of components requires high linear resolution images. Some evidence of this behavior has been found in the jet of 3C 454.3 ([98]), where 43 GHz VLBA observations have revealed the existence of a stationary component that moves downstream slightly before returning back upstream as a moving component passes it. Other evidence has been found in the jets of 3C 120 ([50], [54]), 0735+178 ([30]), 3C 279 ([134]), and may be expected in other sources as more high-frequency images become available.

In [107] the appearance of VLBI knots is studied by obtaining the total intensity emission from relativistic flows computed using the relativistic hydrodynamical code of [25]. Computation of the synchrotron radiation is obtained by computing the emission and absorption coefficients (Eqs. 8 and 9), taking into account opacity effects to integrate the transfer equation (Eq. 10). Time delay effects are ignored because the jet structures are found to move at barely relativistic speeds.

Making use of this numerical model, perturbations in the jet are studied in [107] by introducing a sinusoidal modulation of the inflow Lorentz factor between 1 and 10. Figure 3 shows the obtained density plots before, and after the perturbations are introduced. The relative dominance of the intrinsic emissivity and Doppler boosting in the intensity images is studied by computing the emission at different observing viewing angles. For small viewing angles the image morphology is found to be determined primarily by the Doppler boosting of the high-velocity jet, whereas at larger angles the intrinsic emissivity is more important. Blazars are assumed to be observed along small viewing angles, and therefore the appearance of VLBI knots is determined primarily by the Doppler boosting of fast moving jet perturbations.

3.2 Trailing shocks

The evolution of a strong shock wave cannot ideally be isolated from the underlying jet flow. During its motion along the jet the shock wave interacts with the ambient jet medium, as well as the quiescent flow. This highly non-linear interactions trigger a local pinch instability ([59]) that leads to the formation of a series of conical shocks. Some of these shocks are present in the simulations of Fig. 1 and have been studied in detail by [1].

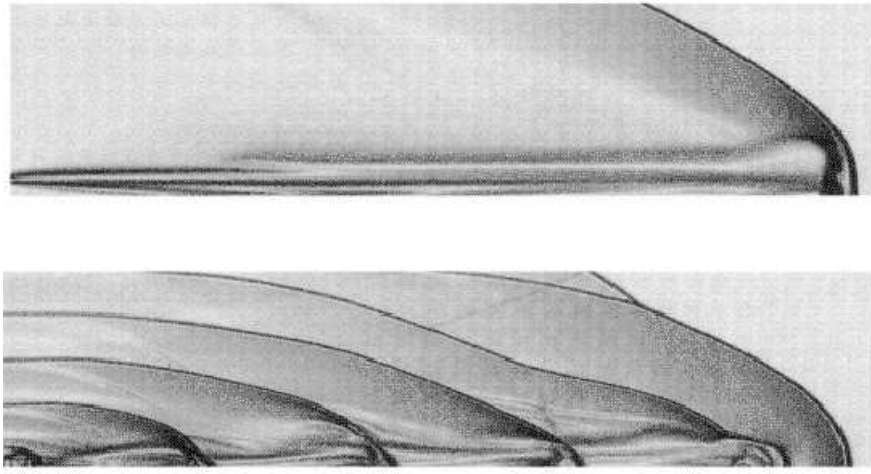


Fig. 3. Schlieren-type images of laboratory frame density gradient for a jet with a Lorentz factor of 10 and adiabatic index of $4/3$. Bottom image shows the same jet after the inflow Lorentz factor has been sinusoidally modulated between 1 and 10 to induce perturbations. Reprinted from [107]

Figure 4 shows the Lorentz factor distribution for a jet simulation after the passage of a strong shock. Multiple conical recollimation shocks (“trailing shocks”) can be found to follow the main perturbation. Although their strength is a function of the distance from the jet inlet, simulated total intensity maps show that they should be strong enough as to be detectable by present VLBI arrays ([1]).

These trailing shocks can be easily distinguished because they appear in the simulated maps as components being released on the wake of primary superluminal component (associated with the leading shock), instead of being ejected from the core of the jet. Those trailing components appearing closer to the core show small apparent motions and a very slow secular decrease in brightness, from which they could be identified as stationary components. Those appearing farther downstream are weaker and can reach superluminal apparent motions. Their oblique nature should also result in different polarization properties from that of the main planar leading shock. The existence of these trailing components indicates that not all observed components necessarily represent a major perturbation at the jet inlet; rather, multiple emission components can be generated by a single disturbance in the jet.

A sample of 42 γ -ray blazars observed at high frequencies with the VLBA has revealed that stationary components are more common than previously thought ([75]). In 27 of those sources at least one non-core stationary component has been observed. By analyzing the properties of these stationary features two different classes of stationary components are established ([75]): those within about

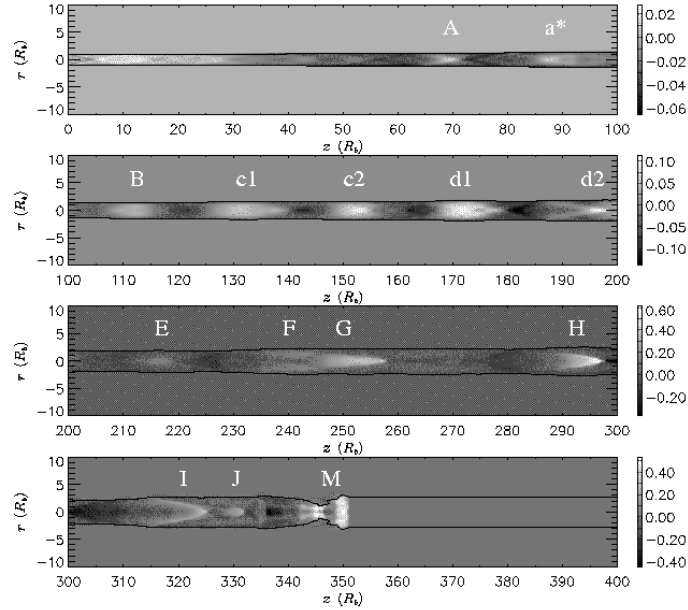


Fig. 4. Relative variation with respect to the quiescent jet of the Lorentz factor (logarithmic scale). Multiple conical recollimation shocks (“trailing shocks”) are found to follow the main shock labeled “M”. Reprinted from [1].

2 mas of the core, probably associated with standing hydrodynamical compressions, and those farther down the jet, probably associated with bends in the jet. These inner stationary features are in good agreement with the properties predicted for the trailing shocks, and therefore their association seems a plausible interpretation for their nature. Polarimetric high resolution VLBI observations should provide the necessary information as to confirm or rule out this hypothesis.

3.3 Jet Instabilities and the Formation of Knots

Relativistic jets in AGNs and microquasars are thought to be subject to instabilities, perhaps due to changes in their feeding from unstable accretion disks. These jet instabilities have been studied with great detail by linear stability analysis of the linearized fluid equations and by non-linear hydrodynamical simulations (e.g., [16], [102], [58], [115], [59], [137]).

Numerical simulations by [137] have revealed that mode–mode interactions in 3D, such as helical surface and helical body mode interactions and coupling to pinch modes, may lead to the formation of relatively stationary knots along the jet beam. In particular, wave–wave interactions are shown to lead to the formation of internal to the jet beam nearly stationary knots close to the jet

inlet, but to move and develop shock spurs at larger distances. These mode-mode interactions, as well as the trailing shocks, may explain some of the puzzling knots evolution observed in the galactic superluminal GRO J1655-40 ([61]).

4 Magnetic Fields in Relativistic Jets

Although recent polarimetric VLBI observations are providing added information on the magnetic field strength and structure at different jet scales, it is still largely unknown the role played by the magnetic field in the jet dynamics. In order to have a dynamically important magnetic field we should look for jet regions where the magnetic pressure $B^2/8\pi$ dominates over the thermal jet plasma pressure. This can be found in the inner jet regions, where magnetic pressure should be of importance for the initial jet formation and collimation.

4.1 Formation, Collimation, and Acceleration of Jets

Observation of the inner jet regions, where jets are formed, collimated and accelerated, requires of the highest possible linear resolution in terms of the black hole Schwarzschild radii, which determines the scale length for the system. It is therefore in nearby sources with known massive central black hole where high frequency VLBI observations can provide the necessary linear resolution. This has been achieved by global 43 GHz VLBI observations of the jet in M87 ([74]), revealing that the strong collimation of the jet takes place at 30-100 Schwarzschild radii (r_s) from the black hole, continuing out to $\sim 1000 r_s$.

Thanks to the development of recent general relativistic magnetohydrodynamic (GRMHD) numerical codes ([79], [80], [81]) it is now possible to study the production of relativistic jet by numerical simulations (see e.g., reviews by [105], [106]). The common scenario for jet production requires a differentially rotating accretion disk surrounding the massive central object. The disk is also threaded with an axial magnetic field of sufficient strength to exert a braking force on the rotating plasma, removing angular momentum and transferring it along the magnetic field lines. These rotating magnetic twists push out and pinch the plasma into a jet. This sweeping pinch mechanism appears to be nearly universal ([106]).

Numerical GRMHD simulations of jet formation in a rapidly rotation Kerr black hole have been performed for the cases of a co-rotating and counter-rotating Keplerian accretion disk ([81], Fig. 5). For the co-rotating disk case, a pressure driven jet is formed by a shock in the disk, together with a weaker magnetically driven jet outside the pressure driven jet. However, for the counter-rotating disk case, a powerful magnetically driven jet is formed inside the pressure driven jet. This magnetically driven jet is accelerated by a strong magnetic field created by frame dragging in the ergosphere of the black hole.

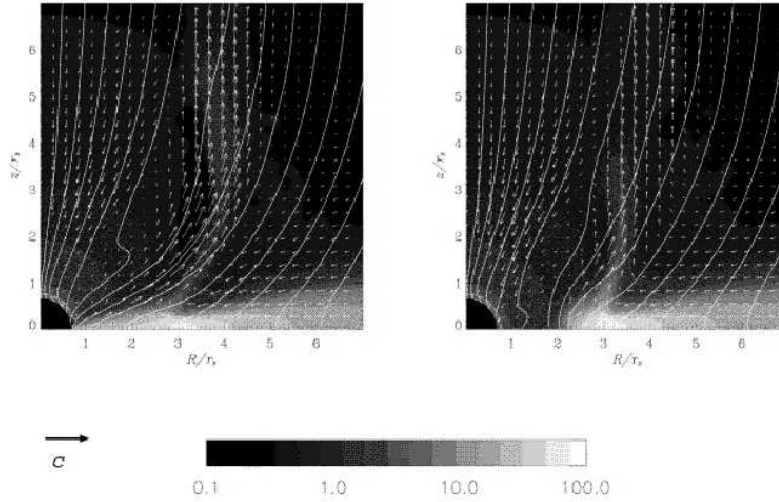


Fig. 5. Numerical models of jet formation for the case of a counter-rotating (left) and co-rotating disk (right). Grey scale shows the logarithm of the proper mass density; vectors indicate velocity; solid lines show the poloidal magnetic field. Reprinted from [81].

4.2 Intrinsic Polarimetric Differences in Jets of AGNs

Polarimetric VLBI observations have revealed intrinsic differences in the jets of BL Lacertae type objects and QSOs that cannot be explained solely by differences in the viewing angle to the flow axis. First evidence for these intrinsic differences were observed in the polarization properties of the jets in the Pearson–Readhead sample through VLBI observations at 6 cm ([29], [21]). These observations have shown that the magnetic fields in BL Lac jet components are commonly perpendicular to the jet structural axis, while for QSOs the orientation is typically aligned to the jet axes. Recent observations ([31], [35], [34]) confirm these differences, but also provide evidence that about 30% of the BL Lac sources in the sample present aligned magnetic fields, similar to those found in QSOs. This difference in the polarization properties of BL Lacs and QSOs is interpreted by associating the observed knots with moving transverse shocks in jets containing mainly tangled magnetic fields. Shocks would be stronger and more commonly observed in BL Lacs, leading to the observed perpendicular fields in the knots. On the contrary, QSOs would be required to be less active, with weaker shocks that would never dominate in polarization.

This larger activity in BL Lacs is also supported by the University of Michigan long-term total and polarization monitoring program ([3]). BL Lacs are found to be more highly variable in total flux than QSOs, and to present quasi simultaneous variations at different frequencies. This also suggests the existence of intrinsic opacity differences between the two classes of objects. The analysis of the polarized light curves is indicative of the existence of propagating shocks

during outbursts. The larger variability in BL Lacs then supports the model in which shock formation is more frequent in BL Lacs parsec-scale jets than in QSOs.

The different activity in these two classes of objects can be interpreted in terms of jet instabilities ([3]). In [115] it is found that higher jet stability can be obtained in faster and colder jet. However, simulations by [102] show that highly supersonic jets (those in which the kinematic relativistic effects due to high Lorentz factors dominate) present a rich internal structure, with multiple internal shocks and extended overpressured cocoons. Both set of simulations ([115], [102]) agree on finding hot jets (i.e., beams with internal energies comparable to the rest-mass energies) the most stable. Further relativistic HD simulations of jet stability are required to explore the space parameters to determine in which cases jets are expected to be more or less stable, and then establish a relationship with the jets in QSOs and BL Lacs (presumably less stable).

It is also possible that this apparent differences in the jet stability of BL Lacs and QSOs depend on the jet scales studied. Higher resolution (1.3 cm and 7 mm) polarimetric VLBI observations ([89], [90]), therefore exploring inner jet regions than those mapped at 6 cm, reveal no significant differences in the polarization properties of BL Lacs and QSOs. Furthermore, comparison between radio and optical reveals a strong correlation in the polarization of the radio core and overall optical polarization of the source, suggesting a common and possibly co-spatial origin for the emission at these frequencies. Magnetic fields perpendicular to the flow direction are commonly observed for the radio cores. Similar orientations are found in the optical, suggesting that the emission at both wavelengths is originated by a strong transverse shock, perhaps the first recollimation shock in the jet, associated with the radio core (see section 3.1).

Although no significant differences in the polarization of BL Lac and QSOs are found in the high resolution observations of [90], the previous dichotomy is translated to high- and low-optically polarized compact radio-loud quasars (HPQs and LPRQs, respectively). LPRQs are found to have components with magnetic fields predominantly parallel to the jet, while in HPQs components tend to have perpendicular magnetic field orientations. This is interpreted assuming that LPRQs represent a quiescent phase of blazar activity, in which the inner jet does not contain strong moving shock waves.

4.3 Intraday Polarization Variability

Rapid variations, with time scales less than a day, in both total and polarized flux density have been observed in several radio sources (see e.g. review by [130]). If intrinsic and resulting from incoherent synchrotron radiation, this intraday variability (IDV) implies jets with bulk Lorentz factors between approximately 30 to 100, larger than the largest values inferred from superluminal motions, and requiring implausibly high brightness temperatures ([15]). Although most IDV at radio wavelengths probably includes some contribution from propagation effects ([114]), recent polarimetric VLBI observations reveal that some of these variations may be intrinsic to the sources ([32], [33], [36]).

One of the first sources found to exhibit IDV is the BL Lac object 0716+714. VLA observations of this source revealed a rotation of the polarization angle by about 50° in 12 hours. By comparison with simulations VLBI observations, it was possible to determine that, contrary to what it was expected, the region responsible for this variability was not the core, but probably a feature located at about 25 milliarcseconds from it ([32]). Further IDV in polarization, but *not* in total flux, have been found in the inner regions of the jets in several other sources, including 0917+624, 0954+658, 1334-127, 2131-021, and 2155-152 ([33], [36]). In the case of 2155-152, IDV variations were seen directly in the polarized intensity images of this source at 5 GHz, where only one of the two polarized milliarcsecond scale features varied. This represents one of the first evidence that IDV in polarization is intrinsic to the source. Although propagation of shocks through turbulent jets may explain some of the observed IDV properties ([95]), further observations and theoretical modeling are necessary to obtain a more detailed picture of the jet physical processes required to explain the exhibited IDV.

5 Jet Environments

Propagation of jets is greatly determined by the distribution of gas in their host galaxies. As the same time, the interaction of the jet with the ambient gas may play an important role in determining some of the observational properties of the emission-line gas. Distinct signs of interaction between a collimated radio jet and a clumpy Narrow Line Region (NLR) are commonly found in the form of morphological associations between radio and optical structures ([18], [28], [10], [129]). The radio-optical association suggests that the interaction of the jets with the interstellar medium strongly influences the dynamics of the ionized gas in the NLR. Furthermore, the ambient gas can be ionized by the direct interaction with the jet bow shock, or by diffuse photoionizing radiation fields produced in the shocks generated by such interactions, as observed in 3C277.3 and 3C171 ([122]).

Exploration of the time-dependent interaction of jets with the NLR have been performed by numerical non-adiabatic hydrodynamical simulations ([119]). These simulations show that the association between the radio and optical emission can be explained as a natural consequence of the expansion of a hot jet cocoon into the interstellar medium. Radiative losses create an envelope of dense cool gas and discrete emission-line knots which can be associated with the narrow-line clouds themselves. Some of these clouds might be partially neutral and represent sites of jet-induced star formation ([119]). Simulated H_α emission shows similar total line widths to those observed in NLR of Seyfert galaxies, presenting large-scale variations in the radial velocities of the clouds due to the stratified pressure in the bow shock region of the jet ([120]).

Direct collisions between the jet and clouds of the BLR and NLR are statistically expected, depending on the assumed values for the cloud sizes and the filling factor (e.g., [92]). Three-dimensional numerical hydrodynamical simula-

tions ([132], [23]) have been used to study direct collisions of a jet with isolated clouds. These simulations show that, although powerful jets would disperse the clouds, for off-center collisions nonaxisymmetric instabilities are induced in the jet and can eventually disrupt it. These interactions could explain some of the morphologies observed in compact steep-spectrum sources, such as the strongly bent geometries found in some of these sources ([92]).

5.1 Jet-cloud Collisions in 3C 120

The radio galaxy 3C 120 was one of the first four sources in which superluminal motion was detected on the scale of parsecs ([118]) to tens of parsecs ([131]). High resolution polarimetric VLBI observations ([50], [52]) have revealed a richer, more rapidly changing structure in total and linearly polarized intensity than that found in other relatively nearby compact extragalactic jets ([74], [125], [76]). Thanks to its proximity ($z=0.033$), millimeter VLBI observations allow to probe the inner jet structure of 3C 120 with very high linear resolution, $\sim 0.1 h_{65}^{-1}$ pc at 43 GHz. This provides enough resolution as to test some of the predictions obtained with the numerical simulations outlined in section 3. Towards this aim, the radio galaxy 3C 120 has been studied with unprecedented spatial and temporal resolution by performing a 16 epoch monthly monitoring with the VLBA at 22 and 43 GHz in dual polarization. This represents the most thorough study of a relativistic jet to date, complete with the highest resolution and polarization ([56]). The obtained sequence of images at 22 GHz is reproduced from [56] in Fig. 6.

The images show the appearance of a new strong superluminal component, labeled “O” in Fig. 6, coincident with a major outburst in the light curve. The passage of this new superluminal component triggered the appearance of a stationary feature (“M” in Fig. 6) that presents also enhanced linearly polarized emission. This behavior is in agreement with the numerical simulations of “trailing shocks” by [1], which explain the appearance of this stationary feature as a consequence of the jet instabilities produced by the passage of the strong leading shock, which would be associated with component “O”.

Figure 7 shows the light curves for several of the components found in 3C 120 where a remarkable brightening can be observed starting when components reach a distance from the core of ~ 2 mas. The most pronounced (in terms of change in flux density) flare corresponds to the component labeled “L”, which increased its total flux density by a factor of 9, becoming the strongest feature in polarized intensity (Fig. 6). This flare is accompanied by rotation of the magnetic vector and an increase in degree of polarization at both, 22 and 43 GHz. The slower rotation of the magnetic vector at 43 GHz reveals a progressive increase in the rotation measure (RM) of component “L”, reaching a value of $\sim 6000 \pm 2400$ rad m^{-2} at peak emission.

The rapid flares in the flux densities of components are followed by equally fast declines when they reach ~ 3 mas from the core. It is difficult to explain such rapid changes in the total and polarized flux density, as well as polarization angle, for components located between a deprojected distance of 4 and 10 pc

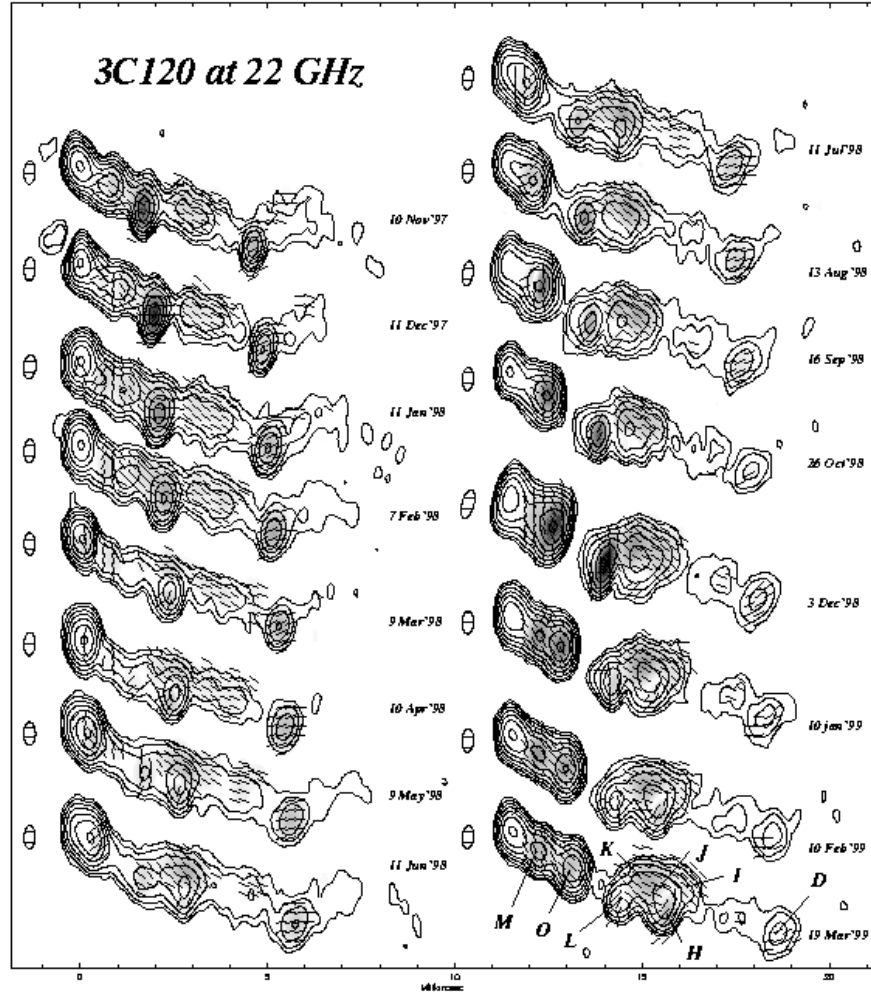


Fig. 6. 16 epoch monthly monitoring of the jet in the radio galaxy 3C 120 obtained with the VLBA at 22 GHz. Total intensity is plotted in contours, linearly polarized intensity in gray scale, and magnetic vectors with bars. Reprinted from [56].

from the core. The bending of the jet appears to be too slight to cause such variations in brightness (from changing relativistic beaming of the radiation relative to the observer) without an accompanying acceleration of the apparent velocity and presence of a stationary component at this site ([2], [45]). Rather, interaction between the jet and a dense cloud in the external medium seems the most plausible explanation. Similar interactions between the jet and interstellar medium were inferred previously from the discovery of an emission-line counterpart to the more extended radio jet in 3C 120 ([62], [9]). It appears that this

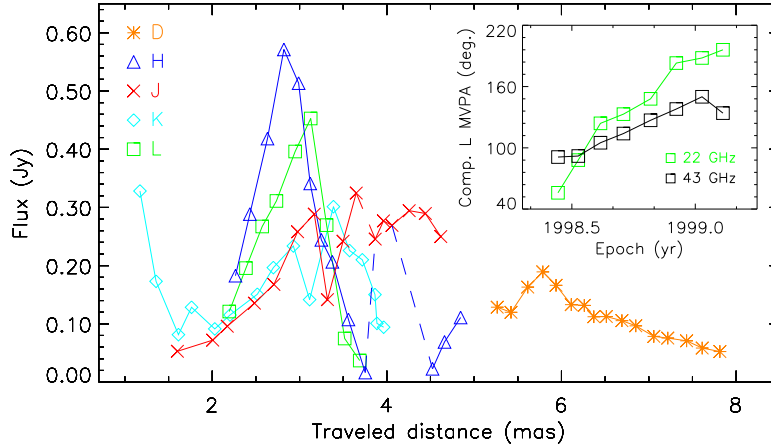


Fig. 7. Light curves for components in the radio galaxy 3C 120 shown in Fig. 6. Inset panel shows the evolution with time of the magnetic vector position angle of component “L”. Reprinted from [56].

interaction is most intense along the southern border of the jet, where the gentle northward curvature causes components with higher than average momentum to collide with the external medium or cloud. Indeed, it is at the beginning of this bend that component “L”, which is the closest to the southern jet border and the one exhibiting the largest flare, began to increase its flux density. This behavior is explained if the magnetic field and population of relativistic electrons in component “L” were enhanced by the shock wave produced by interaction of the jet with the external medium, resulting in a rapid rise in synchrotron emission. The observed increase in the degree of polarization is then explained as a consequence of ordering of the field by the shock wave. The rotation of the magnetic vector observed in component “L” can be interpreted as Faraday rotation, the level of which can be estimated from the different polarization angles observed at 22 and 43 GHz (Fig. 7). After removing this effect, the relative orientation of the magnetic field and velocity vector (which rotates as the component follows the bend in the jet) remains at $40 \pm 10^\circ$. The observed Faraday rotation can be explained by an ionized cloud along the line of sight that may also physically interact with the jet.

For a cloud at a temperature of 10^4K , free-free absorption provide an estimated electron density of $\sim 5 \times 10^4 \text{ cm}^{-3}$. The observed RM of $\sim 6000 \pm 2400 \text{ rad m}^{-2}$ would then require a magnetic field strength of $\sim 0.4 \text{ mG}$. Similarly large RMs have been found in several extragalactic jets ([126], [124], [73]), with estimated magnetic fields of the same order. This electron density and distance from the central engine is intermediate between those of the broad and narrow emission-line clouds in AGNs. Given its high column density, $\sim 6 \times 10^{22} \text{ cm}^{-2}$, such a cloud could be detected in absorption if there is a substantial neutral atomic or molecular component, as expected. Such an observation, which could

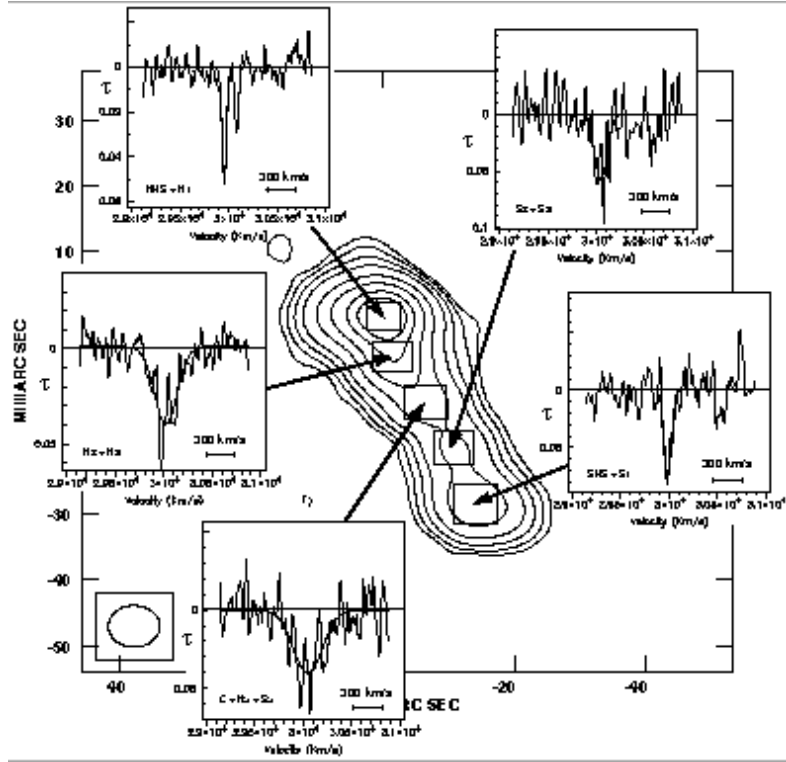


Fig. 8. Integrated profiles of HI absorption in five regions of the compact symmetric object 1946+708. Contours show the radio continuum image at 1.29 GHz. Reprinted from [112].

be carried out with the VLBA in spectral-line mode, would determine the radial velocity of the cloud and therefore whether it is moving toward or away from the central engine.

Spectral-line VLBI observations have allowed to investigate the ambient medium in AGNs with great detail ([108], [123], [40], [112], [110]). The common scenario outlined by these observations consists of an accretion disk or torus surrounding the central engine of the AGN. Depending on the source geometry, part of the jet radio continuum would be absorbed by the atomic gas that mainly comprises the disk, producing the HI absorption lines. The UV photons from the central engine would ionize the inner gas of the AGNs, leading to free-free absorption of the jet radio continuum.

In the compact symmetric object 1946+708, VLBA spectral-line observations ([112]) have revealed narrow HI absorption lines in the jet northern hot spots, indicative of small clouds of warm neutral gas associated with an extended clumpy torus located between the radio jet and the observer (see Fig. 8).

The high velocity dispersion and column density toward the core of 1946+708 suggests fast moving material, possibly in rotation around the central engine.

5.2 Jet Stratification

Propagation of relativistic jets through the ambient medium leads to the formation of shear layers. Such shear layers have been invoked in the past to account for a number of observational characteristics observed in FR I ([87], [88]) and FR II sources ([121]).

One of the best observational evidence for these shear layers have been recently found in the arcsec scale jet of 1055+018 ([8]). Polarization imaging with the VLBA at 6 cm shows that 1055+018 apparently consists of i) a emission spine along the jet axis containing a series of knots in which the magnetic field is predominantly perpendicular to the axis, and ii) a boundary layer in which the magnetic field is predominantly parallel to the axis, as shown in Fig. 9. The aligned magnetic field in the shear layer is assumed to be originated by the jet interaction with the ambient gas. This cross-section asymmetry presents however a rather unusual structure, since it is observed to change with distance along the jet: the shear layer is only visible on one side of the jet at a time.

Three dimensional numerical hydrodynamic and emission simulations have been performed to investigate the formation of shear layers and their implications in the jet emission ([6]). These simulation show that the interaction of the jet with the external medium gives rise to a jet stratification in which a fast spine is surrounded by a slow high-energy shear layer. In order to explore the polarization observational properties of such a jet stratification, [6] considered an ad hoc distribution of the magnetic field consisting of two components: i) a toroidal field present both in the jet spine and the shear layer, and ii) a second component aligned in the shear layer and radial in the jet spine. The resulting projected magnetic field is aligned in the shear layer and is perpendicular in the jet spine, as suggested by several observations ([87], [121], [8]).

Because of this helical magnetic field structure in the shear layer, an asymmetry in the emission is found to appear across the jet. This asymmetry is more pronounced in the polarized emission, and is a function of the viewing angle, as shown in Fig. 10. The synchrotron radiation coefficients are a function of the sine of the angle between the magnetic field and the line of sight in the fluid frame, ϑ (Eqs. 3 and 4). Therefore, asymmetries in the distribution of ϑ will be translated into the emission maps, giving rise to the jet asymmetry. In order to compute ϑ is necessary first to Lorentz transform the line of sight from the observer's, θ , to the fluid's frame θ' (see e.g., [116]). For a helical magnetic field with a pitch angle ϕ , measured with respect to the jet axis, the angles ϑ^t and ϑ^b (where superscripts t and b refer to the top and bottom of the jet, respectively) add 2ϕ (note that $\vartheta^{t,b}$ is always defined as positive). Therefore, as long as ϕ is different from zero or $\pi/2$, i.e. the field is neither purely aligned nor toroidal, the factor $\sin \vartheta^{t,b}$ in the synchrotron radiation coefficients will introduce an asymmetry in the jet emission. This asymmetry will reach a maximum value for a helical magnetic

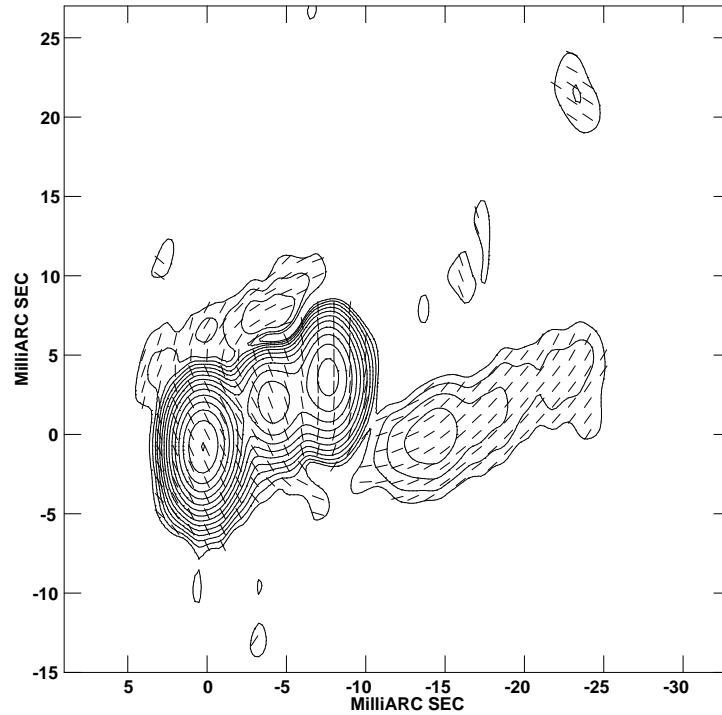


Fig. 9. Linear polarization distribution of the blazar 1055+018 obtained with the VLBA+Y1 at 5 GHz. The ticks show the magnetic vector orientation. Reprinted from [8].

field with $\phi = \pi/4$. However, indistinctly of the helix pitch angle, the predominance between $\sin \vartheta^t$ and $\sin \vartheta^b$ will reverse at $\theta' = \pi/2$, which corresponds to a viewing angle in the observer's frame of $\cos \theta_r = \beta$. For a helical field oriented clockwise as seen in the direction of flow motion (i.e., the aligned component of the field is parallel to the jet flow), and for $\theta' < \pi/2$ the bottom of the jet will show larger emission, while for $\theta' > \pi/2$ the top of the jet will be brighter (the opposite is true for a helical field oriented counter-clockwise, i.e. $\phi > \pi/2$). The maximum asymmetry will be obtained for $\theta' = \phi$ and $\theta' = \pi - \phi$, and the fastest transition (with changing θ') between top/bottom emission predominance will be obtained for ϕ close to $\pi/2$, i.e. when little aligned field is present.

It is interesting to note that for $\theta \sim \theta_r$, small changes in the jet velocity or the viewing angle will produce a flip in the top/bottom jet total and polarized emission dominance. This model has been used by [6] to interpret the shear layer structure observed in 1055+018 ([8]). For this, 1055+018 is required to be oriented close to θ_r and to contain a shear layer with a helical field. In this case, the flip in the top/bottom orientation of the polarization asymmetry in 1055+018

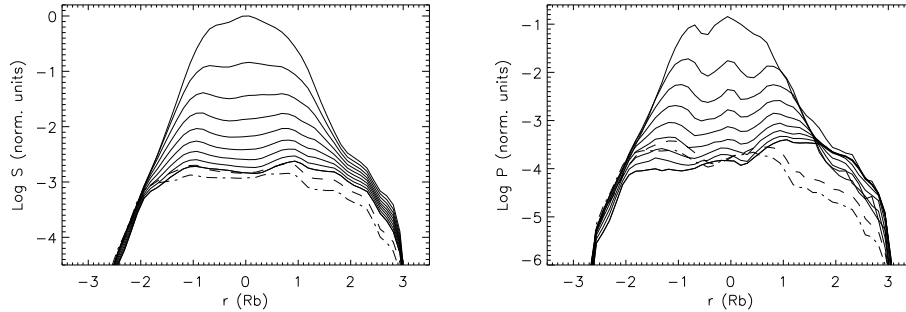


Fig. 10. Logarithm of the integrated total (left) and polarized (right) intensity across the jet for different viewing angles. Lines are plotted in intervals of 10° between an angle of 10° (top line in both plots) and 90° (showing a progressive decrease in emission). Dashed (dot dashed) lines correspond to an observing angle of -130° (-170°). Reprinted from [6].

is interpreted as due to a jet deceleration, as observed for several components in this source ([8]).

6 Conclusions

Numerical relativistic (magneto)hydrodynamic and emission simulations have proven to be a powerful tool to understand the physics of jets in AGNs and microquasars through direct comparison with observations. These models are capable of study the jet dynamics with unprecedented detail, and under similar conditions to those in actual sources (relativistic internal energies and bulk flow velocities). Computation of the non-thermal radio emission allows to study the relationship between radio knots and internal shock waves. These simulations show that the evolution of moving shock waves is greatly determined by its interaction with other standing shock waves, as well as the underlying jet flow and external medium. “Upstream” knot motions, “dragging” of previously stationary components, and formation of multiple “trailing” components after the passage of a main strong shock are some of the predictions obtained from these simulations. First observational evidence of these features are being obtained thanks to the recent millimeter polarimetric VLBI observations.

The dynamical and emission evolution of jet components may be severely affected by interactions with the external medium. An extensive monitoring of the radio galaxy 3C 120 with the highest resolution and in polarization has provided direct imaging of the interaction between jet components and the external medium, resulting in rapid changes in the total and linearly polarized emission of components. These interactions between the jet and ambient medium may also result in a jet stratification, in which a fast spine is surrounded by a slow high-energy shear layer, leading to an emission cross section jet asymmetry.

Further numerical simulations, and its comparison with high resolution observations should provide new insights towards the understanding of the physical processes taking place in the jets of AGNs and microquasars.

References

1. Agudo, I., Gómez, J. L., Martí, J. M., Ibáñez, J. M., Marscher, A. P., Alberdi, A., Aloy, J. M., & Hardee, P. E. 2001, *ApJ*, in press
2. Alberdi, A., Marcaide, J. M., Marscher, A. P., Zhang, Y. F., Elosegui, P., Gómez, J. L., & Shaffer, D. B. 1993, *ApJ*, 402, 160
3. Aller, M. F., Aller, H. D., Hughes, P. A., & Latimer, G. E. 1999, *ApJ*, 512, 601
4. Aloy, M. A., Ibáñez, J. M., Martí, J. M., & Müller, E. 1999, *ApJS*, 122, 151
5. Aloy, M. A., Ibáñez, J. M., Martí, J. M., Gómez, J. L., & Müller, E. 1999, *ApJ*, 523, L125
6. Aloy, M. A., Gómez, J. L., Ibáñez, J. M., Martí, J. M., & Müller, E. 2000, *ApJ*, 528, L85
7. Aloy, M. A., & Martí, J. M. 2001, this proceedings
8. Attridge, J. M., Roberts, D. H., & Wardle, J. F. C. 1999, *ApJ*, 518, L87
9. Axon, D. J., Unger, S. W., Pedlar, A., Meurs, E. J. A., Whitte, D. M., & Ward, M. J. 1989, *Nature*, 341, 631
10. Best, P. N., Carilli, C. L., Garrington, S. T., Longair, M. S., & Röttgering, H. J. A. 1998, *MNRAS*, 299, 357
11. Blandford, R. D., & Rees, M. J. 1974, *MNRAS*, 169, 395
12. Blandford, R. D., & McKee, C. F. 1976, *PhFl*, 19, 1130
13. Blandford, R. D., & Königl, A. 1979, *ApJ*, 232, 34
14. Blandford, R. D., & Levinson, A. 1995, *ApJ*, 441, 79
15. Begelman, M. C., Rees, M. J., & Sikora, M. 1994, *ApJ*, 429, L57
16. Bodo, G., Massaglia, S., Rossi, P., Rosner, R., Malagoli, A., & Ferrari, A. 1995, *A&A*, 303, 281
17. Bowman, M. 1994, *MNRAS*, 269, 137
18. Capetti, A., Axon, D. J., Kukula, M., Macchetto, F., Pedlar, A., Sparks, W. B., & Boksenberg, A. 1995, *ApJ*, 454, L85
19. Cawthorne, T. V. 1991, in *Beams and Jets in Astrophysics*, ed. P. A. Hughes (Cambridge: Cambridge Univ. Press), 187
20. Cawthorne, T. V., & Cobb, W. K. 1990, *ApJ*, 350, 536
21. Cawthorne, T. V., Wardle, J. F. C., Roberts, D. H., & Gabuzda, D. C. 1993, *ApJ*, 416, 519
22. Daly R. A., & Marscher A. P., 1988, *ApJ*, 334, 539
23. de Gouveia Dal Pino, E. M. 1999, *ApJ*, 526, 862
24. Dubal, M. R., & Pantano, O. 1993, *MNRAS*, 261, 203
25. Duncan, G. C., & Hughes, P. A. 1994, *Apj*, 436, L119
26. Eichler, D., & Wiita, P. J. 1978, *Nature*, 274, 38
27. Ferrari, A. 1998, *ARA&A*, 36, 539
28. Fosbury, R. A. E., Morganti, R., Wilson, W., Ekers, R. D., di Serego Alighieri, S., & Tadhunter, C. N. 1998, *MNRAS*, 296, 701
29. Gabuzda, D. C., & Cawthorne, T. V. 1992, in *Variability of Blazards*, ed. E. Valtaoja & M. Valtonen (Cambridge: Cambridge Univ. Press), 238
30. Gabuzda, D. C., Wardle, J. F. C., Roberts, D. H., Aller, M. F., & Aller M. H. 1994, *ApJ*, 435, 128

31. Gabuzda, D. C., Pushkarev, A. B., & Cawthorne, T. V. 1999, MNRAS, 307, 725
32. Gabuzda, D. C., Kochenov, P. Yu., Cawthorne, T. V., & Kollgaard, R. I. 2000, MNRAS, 313, 627
33. Gabuzda, D. C., Kochenov, P. Yu., Kollgaard, R. I., & Cawthorne, T. V. 2000, MNRAS, 315, 229
34. Gabuzda, D. C., & Cawthorne, T. V. 2000, MNRAS, 319, 1056
35. Gabuzda, D. C., Pushkarev, A. B., & Cawthorne, T. V. 2000, MNRAS, 319, 1109
36. Gabuzda, D. C., Kochenov, P. Yu., & Cawthorne, T. V. 2000, MNRAS, 319, 1125
37. Gabuzda, D. C., & Gómez, J. L. 2001, MNRAS, 320, L49
38. Gallant, Y. A., Achterberg, A., & Kirk, J. G. 1999, A&AS, 138, 549
39. Gallant, Y. 2001, these proceedings
40. Gallimore, J. F., Holloway, A. J., Pedlar, A., & Mundell, C. G. 1998, A&A, 333, 13
41. García-Miró, C., Gómez, J. L., & Alberdi, A. 1999, A&A, 351, 147
42. Giovanoni, P. M., & Kazanas, D. 1990, Nature, 345, 319
43. Gómez, J. L., Alberdi, A., & Marcaide, J. M. 1993, A&A, 274, 55-68
44. Gómez, J. L., Alberdi, A., & Marcaide, J. M. 1994, A&A, 284, 51
45. Gómez, J. L., Alberdi, A., Marcaide, J. M., Marscher, A. P., & Travis, J. P. 1994, A&A, 292, 33-44
46. Gómez, J. L., Martí, J. M., Marscher, A. P., Ibáñez, J. M., & Marcaide, J. M. 1995, ApJ, 449, L19
47. Gómez, J. L., Martí, J. M., Marscher, A. P., Ibáñez, J. M., & Marcaide, J. M. 1996, in ASP Conf. Ser. 100, Energy Transport in Radio Galaxies and Quasars, ed. P. E. Hardee, A. H. Bridle, & J. A. Zensus (San Francisco: ASP), p. 159
48. Gómez, J. L., Marscher, A. P., Martí, J. M., & Ibáñez, J. M. 1996, in Blazar Continuum Variability, ed. H. R. Miller, J. R. Webb, and J. C. Noble, p. 242
49. Gómez, J. L., Martí, J. M., Marscher, A. P., Ibáñez, J. M., & Alberdi, A. 1997, ApJ, 482, L33
50. Gómez, J. L., Marscher, A. P., Alberdi, A., Martí, J. M., & Ibáñez, J. M. 1998, ApJ, 499, 221
51. Gómez, J. L., Marscher, A. P., Alberdi, A., & Gabuzda, D. C. 1999, ApJ, 519, 642
52. Gómez, J. L., Marscher, A. P., & Alberdi, A. 1999, ApJ, 521, L29
53. Gómez, J. L., Marscher, A. P., & Alberdi, A. 1999, ApJ, 522, 74
54. Gómez, J. L., Marscher, A. P., Alberdi, A., Martí, J. M., Ibáñez, J. M., & Marchenko, S. G. 1999, in ASP Conf. Ser. 159, BL Lac Phenomenon, ed. L. O. Takalo, & A. Sillanpää (San Francisco ASP), 435
55. Gómez, J. L., & Marscher, A. P. 2000, ApJ, 530, 245
56. Gómez, J. L., Marscher, A. P., Alberdi, A., Jorstad, S. G., & García-Miró, C. 2000, Science, 289, 2317
57. Gómez, J. L. 2001, in Galactic Relativistic Jet Sources, ed. A. J. Castro-Tirado, J. Greiner, J. M. Paredes, Astrophysics and Space Science, in press
58. Hardee, P. E., Rose, A., Hughes, P. A., & Duncan, G. C. 1998, ApJ, 500, 599
59. Hardee, P. E. 2000, ApJ, 533, 176
60. Homan, D. C., & Wardle, J. F. C. 1999, AJ, 118, 1942
61. Hjellming, R. M., & Rupen, M. P. 1995, Nature, 375, 464
62. Hua, C. T. 1988, A&A, 199, 105
63. Hughes, P. A., Aller, H. D., & Aller, M. F. 1985, ApJ, 298, 301
64. Hughes, P. A., Aller, H. D., & Aller, M. F. 1989, ApJ, 341, 54
65. Hughes, P. A., Aller, H. D., & Aller, M. F. 1991, ApJ, 374, 57

66. Hughes, P. A., Duncan, C., & Mioduszewski, A. 1996, in ASP Conf. Ser. 100, Energy Transport in Radio Galaxies and Quasars, ed. P. E. Hardee, A. H. Bridle, & J. A. Zensus (San Francisco: ASP), p. 137
67. Hughes, P. A. 2000, in ASP Conf. Ser. 201, Particles and Fields in Radio Galaxies, ed. R. A. Laing, & K. M. Blundell (San Francisco: ASP). Available as [astro-ph/0011127](#)
68. Jones, T. W., & O'Dell, S. L. 1997, *ApJ*, 214, 522
69. Jones, T. W., & O'Dell, S. L. 1997, *ApJ*, 215, 236
70. Jones, T. W. 1988, *ApJ*, 332, 687
71. Jones, T. W., Ryu, D., & Engel, A. 1999, *ApJ*, 512, 105
72. Junor, W., & Biretta, J. A. 1995, *AJ*, 109, 500-506
73. Junor, W., Salter, D. J., Saikia, D. J., Mantovani, F., & Peck, A. B. 1999, *MNRAS*, 308, 955
74. Junor, W., Biretta, J. A., & Livio, M. 1999, *Nature*, 401, 891
75. Jorstad, S. G., Marscher, A. P., Mattox, J. R., Wehrle, A. E., Bloom, S. D., & Yurchenko, A. V. 2001, *ApJS*, in press
76. Kellermann, K. I., Vermeulen, R. C., Zensus, J. A., & Cohen, M. H. 1998, *AJ*, 115, 1295
77. Kirk, J. G., Rieger, F. M., & Mastichiadis, A. 1998, *A&A*, 333, 452
78. Kirk, J. G., Guthmann, A. W., Gallant, Y. A., & Achterberg, A. 2000, *ApJ*, 542, 235
79. Koide, S., Shibata, K., & Kudoh, T. 1998, *ApJ*, 495, L63
80. Koide, S., Shibata, K., & Kudoh, T. 1999, *ApJ*, 522, 727
81. Koide, S., Meier, D. L., Shibata, K., & Kudoh, T. 2000, *ApJ*, 536, 668
82. Komissarov, S. S., Falle, S. A. E. G. 1996, in *Blazar Continuum Variability*, ed. H. R. Miller, J. R. Webb, and J. C. Noble, p. 173
83. Komissarov, S. S., & Falle, S. A. E. G. 1997, *MNRAS*, 288, 833
84. Komissarov, S. S. 1999, *MNRAS*, 308, 1069
85. Königl, A. 1981, *ApJ*, 243, 700
86. Krichbaum, T. P., Hummel, C. A., Quirrenbach, A., Schalinski, C. A., & Witzel, A. 1990, *A&A*, 230, 271
87. Laing, R. A. 1996, in ASP Conf. Ser. 100, Energy Transport in Radio Galaxies and Quasars, ed. P. E. Hardee, A. H. Bridle, & J. A. Zensus (San Francisco: ASP), 241
88. Laing, R. A. Parma, P., de Ruiter, H. R., & Fanti, R. 1999, *MNRAS*, 306, 513
89. Lister, M. L., Marscher, A. P., & Gear, W. K. 1998, *ApJ*, 504, 702
90. Lister, M. L., & Smith, P. S. 2000, *ApJ*, 541, 66
91. Mannheim, K. 1993, *A&A*, 269, 67
92. Mantovani, F., Junor, W., Bondi, M., Cotton, W., Fanti, R., Padrielli, L., Nicolson, G. D., & Salerno, E. 1998, *A&A*, 332, 10
93. Marscher, A. P. 1980, *ApJ*, 235, 386
94. Marscher, A. P., & Gear, W. K. 1985, *ApJ*, 298, 114-127
95. Marscher, A. P., Gear, W. K., & Travis, J. P. 1992, in *Variability of Blazars*, ed. E. Valtaoja, & M. Valtonen (Cambridge: Cambridge Univ. Press), 85
96. Marscher, A. P. 1996, in ASP Conf. Ser. 100, Energy Transport in Radio Galaxies and Quasars, ed. P. E. Hardee, A. H. Bridle, & J. A. Zensus (San Francisco: ASP), 45
97. Marscher, A. P. 1996, in ASP Conf. Ser. 110, Blazar Continuum Variability, ed. H. R. Miller, J. R. Webb, & J. C. Noble (San Francisco: ASP), 248
98. Marscher, A. P. 1998, in ASP Conf. Ser. 144, Radio Emission from Galactic and Extragalactic Compact Sources, ed. J. A. Zensus, G. B. Taylor, & J. M. Wroble (San Francisco ASP), 25

99. Martí, J. M., Müller, E., & Ibáñez, J. M. 1994, *A&A*, 281, L9
100. Martí, J. M., Müller, E., Font, J. A., & Ibáñez, J. M. 1995, *ApJ*, 448, L105
101. Martí, J. M. 1997, in *Relativistic Jets in AGNs*, ed. M. Ostrowski, M. Sikora, G. Madejski & M. Begelman, *Astronomical Observatory of the Jagiellonian University*, p. 90
102. Martí J. M., Müller E., Font J. A., Ibáñez, J. M., Marquina A., 1997, *ApJ*, 479, 151
103. Martí, J. M., & Müller, E. 1999, *Living Reviews in Relativity*, <http://www.livingreviews.org/Articles>
104. Martí, J. M. 2000, in *AGNs in their Cosmical Environment*, eds. B. Rocca-Volmerange, & H. Sol, *EDP Series in Astronomy and Astrophysics (EDP Sciences)*, in press
105. Meier, D. L. 2001, in *Galactic Relativistic Jet Sources*, ed. A. J. Castro-Tirado, J. Greiner, J. M. Paredes, *Astrophysics and Space Science*, in press
106. Meier, D. L., Koide, S., & Uchida, Y. 2001, *Science*, 291, 84
107. Mioduszewski, A. J., Hughes, P. A., & Duncan, G. C. 1997, *ApJ*, 476, 649
108. Mundell, C. G., Pedlar, A., Baum, S. A., O’Dea, C. P., Gallimore, J. F., & Brinks, E. 1995, *MNRAS*, 272, 355
109. Norman, M. L. 1996, in *ASP Conf. Ser. 100, Energy Transport in Radio Galaxies and Quasars*, ed. P. E. Hardee, A. H. Bridle, & J. A. Zensus (San Francisco: ASP), p. 405
110. Oosterloo, T. A., Morganti, R., Tzioumis, A., Reynolds, J., King, E., McCulloch, P., & Tsvetanov, Z. 2000, *AJ*, 119, 2085
111. Pacholczyk, A. G., 1970. *Radio Astrophysics*. Freeman, San Francisco
112. Peck, A. B., Taylor, G. B., & Conway, J. E. 1999, *ApJ*, 521, 103
113. Rayburn, D. R. 1977, *MNRAS*, 179, 603
114. Rickett, B. J., Quirrenbach, A., Wegner, R., Krichbaum, T. P., & Witzel, A. 1995, *A&A*, 293, 479
115. Rosen, A., Hughes, P. A., Duncan, G. C., & Hardee, P. E. 1999, *ApJ*, 516, 729
116. Rybicki, G., Lightman, A. 1979, *Radiative Processes in Astrophysics*. Wiley, New York
117. Salvati, M., Spada, M., & Pacini, F. 1998, *ApJ*, 495, L19
118. Seielstad, G. A., Cohen, M. H., Linfield, R. P., Moffet, A. T., Romney, J. D., Schilizzi, R. T., & Shaffer, D. B. 1979, *ApJ*, 229, 53
119. Steffen, W., Gómez, J. L., Williams, R. J. R., Raga, A. C., & Pedlar, A. 1997, *MNRAS*, 286, 1032
120. Steffen, W., Gómez, J. L., Raga, A. C. & Williams, R. J. R. 1997, *ApJ*, 491, L73
121. Swain, M. R., Bridle, A. H., & Baum, S. A. 1998, *ApJ*, 507, L29
122. Tadhunter, C. N., Villar-Martín, M., Morganti, R., Bland-Hawthorn, J., & Axon, D. 2000, *MNRAS*, 314, 849
123. Taylor, G. B. 1996, *ApJ*, 470, 394
124. Taylor, G. B. 1998, *ApJ*, 506, 637
125. Tingay, S. J. et al. 1995, *Nature*, 374, 14
126. Udomprasert, P. S., Taylor, G. B., Pearson, T. J., Roberts, D. H. 1997, *ApJ*, 483, L9
127. van Putten, M. H. P. M. 1993, *ApJ*, 408, L21
128. van Putten, M. H. P. M. 1996, *ApJ*, 467, L56
129. Villar-Martín, M., Tadhunter, C., Morganti, R., Clark, N., Killeen, N., & Axon, D. 1998, *A&A*, 332, 479
130. Wagner, S. J., & Witzel, A. 1995, *ARA&A*, 33, 163

131. Walker, R. C. 1997, *ApJ*, 488, 675
132. Wang, Z., Wiita, P. J., & Hooda, J. S. 2000, *ApJ*, 534, 201
133. Wardle, J. F. C., Homan, D. C., Ojha, R., & Roberts, D. H. 1998, *Nature*, 395, 457
134. Wehrle A. E. et al., 1997, in *ASP Conf. Ser. 110, Blazar Continuum Variability*, ed. H. R. Miller, J. R. Webb, & J. C. Noble (San Francisco: ASP), 430
135. Wilson, M. J., & Scheuer, P. A. G. 1983, *MNRAS*, 205, 449
136. Wilson, M. J. 1987, *MNRAS*, 226, 447
137. Xu, J., Hardee, P. E., & Stone, J. M. 2000, *ApJ*, 543, 161